Fourier Spectral Simulations and Gegenbauer Reconstructions for Electromagnetic Waves in the Presence of a Metal Nanoparticle

M. S. Min* T. W. Lee† P. F. Fischer‡ S. K. Gray§

November 30, 2004

Abstract

We describe Fourier pseudospectral time-domain simulations, carried out in order to study light interacting with a metallic nanoscale object. The difficulty of using Fourier methods to accurately predict the electromagnetic scattering in such dielectric configuration arises from the discontinuity in the dielectric function along the surface of the metallic object. Standard Fourier methods lead to oscillatory behavior in approximating solutions that are nonsmooth or that have steep gradients. By applying the Gegenbauer reconstruction technique as a postprocessing method to the Fourier pseudospectral solution, we successfully reduce the oscillations after postprocessing.

Our computational results, including comparison with finite-difference time-domain simulations, demonstrate the efficiency and accuracy of the method.

Keywords. Fourier pseudospectral method, Gegenbauer reconstruction, postprocessing

1 Introduction

Metallic nanostructures, such as metal nanoparticles and nanoholes in thin metal films, are of considerable interest because of the possibility of creating surface plasmon excitations when interacting with light [2], [22]. Surface plasmons are collective electronic excitations that effectively concentrate and confine light energy [4]. The manipulation of surface plasmons could lead to novel nanoscale optoelectronic devices.

Numerical simulations help us to understand and predict the basic physics of such nanophotonics problems and also provide cost-effective tools for prototyping design of potential devices. Among general computational techniques employed in such simulations, Fourier methods have been naturally considered for problems with periodic features, such as planar waveguides and photonic crystal structures for integrated photonic devices. Computational implementations and their error estimates have been analyzed in the literature [8], [25]. In this paper we show how such Fourier methods can be applied to light interacting with metal nanostructures that do not possess periodic features. Our focus is on mathematical reconstruction techniques for Fourier pseudospectral simulation data, using Fourier–Padé and Gegenbauer approximations [15], [20], [23], [25], [26].

As a first step, we study light interacting with a small metallic cylinder or nanowire of diameter of 50 nm and infinite length in a vacuum. Before presenting detailed mathematical formulae, we give a brief overview of the mechanism behind surface plasmon excitation in such a system. Imagine the circular cross section of the nanowire to be in the x–y plane with its long axis parallel to the z–axis. Incident light traveling along x axis with y–polorization is then capable of inducing dipolar (and higher order) charge oscillations

*Mathematics and Computer Science Division, Argonne National Laboratory, Argonne, IL, 60439, USA (mmin@mcs.anl.gov).
†Chemistry Division, Argonne National Laboratory, Argonne, IL, 60439, USA (twlee@tcg.anl.gov).
‡Mathematics and Computer Science Division, Argonne National Laboratory, Argonne, IL, 60439, USA (fischer@mcs.anl.gov).
§Chemistry Division, Argonne National Laboratory, Argonne, IL, 60439, USA (gray@tcg.anl.gov).

near the metal surfaces. These charge oscillations are associated with collective excitations of electrons near the metal surfaces and can lead to electromagnetic surface waves that are highly localized (evanescent) near surfaces, i.e. surface plasmons. A complex–valued dielectric constant is used to discribe the metallic response to radiation. More detailed analysis shows that this dielectric constant must have a negative real part for surface plasmons to be reasonably excited. Absorption of radiation by the metal can also occur which involves introducing an imaginary part to the dielectric constant. In addition to being highly localized, the field intensities of surface plasmon excitations can be extremely large near the metal surfaces.

There are many approaches for solving the relevant Maxwell's wave equations. In this paper we are concerned with time–domain methods that involve grids in space and time. The advantages of such methods include conceptual simplicity and the ability to model a variety of complex system architectures. The most popular time–domain approach is the finite–difference time–domain (FDTD) method [30], [29]. It involves low–order finite differencing to accomplish both spatial and time derivatives. In order to describe surface plasmon behavior accurately, however, very fine grids in both space and time are required. An alternative to FDTD that can lead to better accuracy with larger grid spacings would be to evaluate the spatial derivatives with Fourier methods. Such pseudospectral time–domain (PSTD) methods have been proposed and studied in the context of non–plasmonic systems [20], [26]. However the abrupt, sharp changes in magnitudes of the electromagnetic fields near the metal surfaces due to surface plasmons is problematic for PSTD methods. In particular, nonphysical oscillations called Gibbs oscillations can occur that contaminate the solution over a wide range of coordinate space. However, the finite Fourier data contains enough information about the original solution that one can reexpress the data as a Padé or Gegenbauer finite expansion and can thus reduce the oscillations. In both cases, the reconstructions require obtaining the coefficients for the reconstructed approximations in terms of the Fourier coefficients. Implementations with Fourier–Padé reconstructions in [25] have successfully reduced the oscillations for Fourier pseudospectral solutions of nonlinear partial differential equations such as Burgers' and Boussinesq equations. The Gegenbauer reconstructions have been applied to medical projection data computed by Fourier methods [23]. Here we apply the Gegenbauer reconstruction to Fourier pseudospectral time-domain simulations [20] of Maxwell's equations. The computational results show that the Gegenbauer reconstructions successfully reduce the noise in the Fourier pseudospectral simulations.

This paper is organized as follows. Section 2 gives the formulation of Maxwell's equations and the auxiliary differential equation [17], [29] for the current term from the Drude model. Section 3 presents our numerical discretizations in space and time and the setup of parameters for PSTD simulations. Section 4 introduces the Gegenbauer polynomials and the postprocessing technique (i.e., the Gegenbauer reconstruction procedure) in one dimension. Their convergence behaviors are demonstrated for a nonperiodic analytic function, some discontinuous functions, and a piecewise analytic function. CPU times for simulations will be also discussed. Section 5 presents the implementation in two dimensions. Section 6 demonstrates the reconstructed results of the Fourier pseudospectral solutions from the nanoparticle scattering simulations. FDTD results computed on very finer grids are also provided for comparison with reconstructed results. Section 7 discusses the remaining issues concerning parameter optimizations for the reconstructions and computational automation with an appropriate error estimate. Section 8 briefly summarizes our research.

2 Maxwell's Equations for Metal Nanoparticles

We consider the electrodynamics of metal nanosystem such as those in [2], [4], [17], [18], [22] which are composed of (non–magnetic) metals and dielectric materials. The frequency–domain Maxwell's equations for the electric and magnetic field vectors, $\tilde{E}$ and $\tilde{H}$, may then be taken to be [4]

$$-i\omega\epsilon\tilde{E} = \nabla \times \tilde{H}, \tag{1}$$

$$i\omega\mu_0\tilde{H} = \nabla \times \tilde{E}, \tag{2}$$

where ω is the temporal frequency and μ_0 is the magnetic permeability. Each specific system is defined by the spatial and frequency dependence of the dielectric constant ϵ. Dielectric regions of space can often be described by a positive, real and frequency–dependent dielectric constant. Metallic regions involve a generally complex–valued frequency–dependent dielectric constant. Moreover, the real part of the metallic

dielectric constant can be negative, which is essential for surface plasmon behavior. This latter property can lead to instability in naive time–domain formulations of equation (1).

To address the difficulties noted above, we implement a Drude model [4] of the metallic dielectric constant within an auxiliary differential equation approach [29], as outlined in more detail in [17]. For metallic regions, we first reexpress $\epsilon = \epsilon_0 \epsilon_p$ as

$$\epsilon = \epsilon_0 \left[\epsilon_\infty + (\epsilon_p - \epsilon_\infty)\right], \tag{3}$$

where ϵ_0 the permittivity of free space, ϵ_∞ is the infinite frequency value for the dielectric constant, and ϵ_p will be specified later. Identifying the current density as

$$\tilde{J} = -i\epsilon_0(\epsilon_p - \epsilon_\infty)\tilde{E}, \tag{4}$$

we rewrite equation (1) as

$$\tilde{J} - i\omega\epsilon_0\epsilon_p\tilde{E} = \nabla \times \tilde{H}. \tag{5}$$

Inverse Fourier transforming (5) gives

$$J(t) + \epsilon_0\epsilon_\infty \frac{\partial E(t)}{\partial t} = \nabla \times H(t). \tag{6}$$

The following is the Drude model [4], [17], [29] for the optical properties of a free-electron metal:

$$\epsilon_p = \epsilon_\infty - \frac{\omega_p^2}{\omega^2 + i\Gamma_p}, \tag{7}$$

where Γ_p is the Drude damping coefficient and ω_p is the plasmon frequency. This leads to

$$\frac{\partial^2 J(t)}{\partial t^2} + \Gamma_p \frac{\partial J(t)}{\partial t} = \epsilon_0\omega_p^2 \frac{\partial E(t)}{\partial t}. \tag{8}$$

Reducing the order of the ordinary differential equation, we have

$$\frac{\partial J(t)}{\partial t} + \Gamma_p J(t) = \epsilon_0\omega_p^2 E(t). \tag{9}$$

Equipped with equation (9) for the current term, we define the governing time-domain equations as

$$\epsilon\frac{\partial E}{\partial t} = \nabla \times H - J, \tag{10}$$

$$\mu\frac{\partial H}{\partial t} = -\nabla \times E, \tag{11}$$

$$\frac{\partial J}{\partial t} = \alpha J + \beta E, \tag{12}$$

where the phenomenological parameters in free space are

$$\epsilon = \epsilon_0, \quad \mu = \mu_0, \quad \alpha = 0, \quad \text{and} \quad \beta = 0 \tag{13}$$

and in the metallic region are

$$\epsilon = \epsilon_0\epsilon_\infty, \quad \mu = \mu_0, \quad \alpha = -\Gamma_p, \quad \text{and} \quad \beta = \epsilon_0\omega_p^2. \tag{14}$$

The values for the coefficients ϵ_∞, Γ_p, and ω_p will be assigned by experimental measurement [17].

The electromagnetic field vectors and the current vector are generally written by decomposing each component as follows:

$$E = (E_x, E_y, E_z), \quad H = (H_x, H_y, H_z), \quad \text{and} \quad J = (J_x, J_y, J_z). \tag{15}$$

Here we consider the transverse-electric mode in two dimensions:

$$E = (E_x, E_y, 0), \quad H = (0, 0, H_z), \quad \text{and} \quad J = (J_x, J_y, 0). \tag{16}$$

Then the governing equations (10)-(11) are written as

$$\frac{\partial F}{\partial t} = A\frac{\partial F}{\partial x} + B\frac{\partial F}{\partial y} + CF, \tag{17}$$

where the field vector is $F = [E_x, E_y, H_z, J_x, J_y]^T$ and the coefficient matrices are

$$A = \begin{bmatrix} 0 & 0 & 0 & 0 & 0 \\ 0 & 0 & -\frac{1}{\epsilon} & 0 & 0 \\ 0 & -\frac{1}{\mu} & 0 & 0 & 0 \\ 0 & 0 & 0 & 0 & 0 \\ 0 & 0 & 0 & 0 & 0 \end{bmatrix}, B = \begin{bmatrix} 0 & 0 & \frac{1}{\epsilon} & 0 & 0 \\ 0 & 0 & 0 & 0 & 0 \\ \frac{1}{\mu} & 0 & 0 & 0 & 0 \\ 0 & 0 & 0 & 0 & 0 \\ 0 & 0 & 0 & 0 & 0 \end{bmatrix}, \text{ and } C = \begin{bmatrix} 0 & 0 & 0 & 0 & 0 \\ 0 & 0 & 0 & 0 & 0 \\ 0 & 0 & 0 & 0 & 0 \\ \beta_x & 0 & 0 & \alpha_x & 0 \\ 0 & \beta_y & 0 & 0 & \alpha_y \end{bmatrix}.$$

One can check the well-posedness of this formulation. Equation (12) contains no spatial derivatives and hence it is indeed an ODE for J. After the undifferentiated terms in equation (17) are dropped, it becomes a 3×3 Maxwell system. One can symmetrize it through the following change of variables [16]

$$G = (E_x, E_y, \sqrt{\mu/\epsilon} H_z). \tag{18}$$

Thus the system is symmetric hyperbolic and therefore strongly well-posed [7].

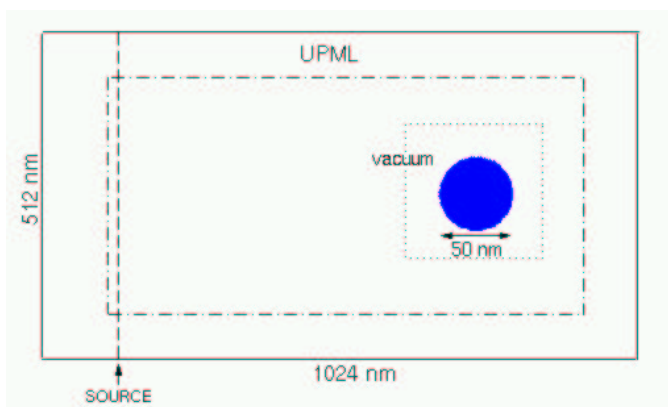

Figure 1: Finite computational domain on $[0, 1024] \times [0, 512]$ nm^2.

3 Numerical Scheme

Let us define the computational domain on $[0, L_x] \times [0, L_y]$, where $L_x = 1024$ nm and $L_y = 512$ nm. The grid points are defined by

$$x_i = \frac{L_x i}{N_x} (i = 0, ..., N_x - 1) \quad \text{and} \quad y_j = \frac{L_y j}{N_y} (j = 0, ..., N_y - 1). \tag{19}$$

Consider a metal cylinder with radius 25 nm whose center is placed at $x = 767.5$ nm and $y = 255.5$ nm in the computational domain (see Figure 1). The parameters of the equations in (14) for the metallic region are chosen as $\epsilon_\infty = 8.926$, $\Gamma_p = -3.08 \times 10^{14}$ Hz, and $\omega_p = 1.7577 \times 10^{16}$ Hz, as in [17], [18]. Since we simulate

infinite-space solutions on a finite computational domain, we introduce an artificial absorbing layer in order to avoid the reflection from outgoing waves. The thickness of the absorbing layer is set to 28 nm and 40 nm in the x- and y-direction, respectively. We use the uniaxial perfectly matched layer (UPML) formulation [27], [29]; in this region the field intensity vanishes as it reaches to the boundary of the computational domain. Thus, it is reasonable to consider this problem as a periodic problem and to apply Fourier approximations globally in the computational domain.

The pseudospectral time–domain (PSTD) scheme [12], [13] we use involves second order explicit leap-frogging in time, just as ordinary FDTD, but replaces the spatial derivatives by the Fourier pseudospectral differentiation operators, denoted by D_x and D_y below. At the time level $t^n = n\Delta t$, our scheme is written as follows:

$$\bar{\epsilon}\frac{\bar{E}_x^{n+\frac{1}{2}} - \bar{E}_x^{n-\frac{1}{2}}}{\Delta t} = D_y \bar{H}_z^n - \bar{J}_x^n, \tag{20}$$

$$\bar{\epsilon}\frac{\bar{E}_y^{n+\frac{1}{2}} - \bar{E}_y^{n-\frac{1}{2}}}{\Delta t} = -D_x \bar{H}_z^n + \bar{J}_y^n, \tag{21}$$

$$\bar{\mu}\frac{\bar{H}_z^{n+1} - \bar{H}_z^n}{\Delta t} = D_y \bar{E}_x^{n+\frac{1}{2}} - D_x \bar{E}_y^{n+\frac{1}{2}}, \tag{22}$$

$$\frac{\bar{J}_x^{n+1} - \bar{J}_x^n}{\Delta t} = \bar{\alpha}\frac{\bar{J}_x^{n+1} + \bar{J}_x^n}{2} + \bar{\beta}\bar{E}_x^{n+1/2}, \tag{23}$$

$$\frac{\bar{J}_y^{n+1} - \bar{J}_y^n}{\Delta t} = \bar{\alpha}\frac{\bar{J}_y^{n+1} + \bar{J}_y^n}{2} + \bar{\beta}\bar{E}_y^{n+1/2}, \tag{24}$$

where the vector representations of the fields and parameters are defined, respectively, by

$$\bar{E}_x^n = [(E_x)_{00}, (E_x)_{10}, ..., (E_x)_{ij}, ..., (E_x)_{N_x-1N_y-1}]^T \quad \text{for} \quad (E_x)_{ij} = E_x(x_i, y_j), \tag{25}$$

$$\bar{\epsilon} = \bar{\epsilon}_{ij} = \epsilon(x_i, y_j), \quad \bar{\alpha} = \bar{\alpha}_{ij} = \alpha(x_i, y_j) \quad \text{and} \quad \bar{\beta} = \bar{\beta}_{ij} = \beta(x_i, y_j). \tag{26}$$

Note that a common, evenly spaced nonstaggered spatial grid is assumed for all field variables which is simpler than the FDTD/Yee [30] gridding scheme.

3.1 Spatial Derivative

The Fourier pseudospectral differentiation operator in two dimensions in (20)–(24) can be represented by using a one-dimensional derivative operator. Let us consider a smoothly differentiable function $f(x)$ with period 2π, specified at N discrete grid points $x_0, ..., x_{\hat{i}}, ..., x_{N-1}$, where $x_{\hat{i}} = 2\pi\hat{i}/N$. Fourier pseudospectral approximation of the function $f(x)$ is defined by

$$f_N(x) = \sum_{\hat{i}=0}^{N-1} f(x_{\hat{i}})\Pi_{\hat{i}}(x), \tag{27}$$

where $\Pi_{\hat{i}}(x_{\hat{j}}) = \delta_{\hat{i}\hat{j}}$ and $\Pi_{\hat{i}}(x)$ is a Lagrange interpolation polynomial of degree N [12]. The polynomials $\Pi_{\hat{i}}(x)$ are given explicitly by

$$\Pi_{\hat{i}}(x) = \frac{1}{N}\sin\left[N(x - x_{\hat{i}})/2\right]\cot\left[(x - x_{\hat{i}})/2\right]. \tag{28}$$

In the pseudospectral method, the first derivatives $df_N(x)/dx$ at the grid points $x_{\hat{j}}$ are obtained in terms of the values $f(x_{\hat{i}})$ by simply differentiating (27):

$$\frac{df_N(x_{\hat{j}})}{dx} = \sum_{\hat{i}=0}^{N-1} f(x_{\hat{i}})\frac{d\Pi_{\hat{i}}(x_{\hat{j}})}{dx} = (\hat{D}f)_{\hat{j}}, \tag{29}$$

where $\hat{D}$ is a $N \times N$ matrix with elements

$$(\hat{D})_{\hat{j}\hat{i}} = \frac{d\Pi_{\hat{i}}(x_{\hat{j}})}{dx} = \begin{cases} 0 & (\hat{i} = \hat{j}) \\ \frac{(-1)^{\hat{i}+\hat{j}}}{2} \cot(x_{\hat{i}} - x_{\hat{j}}) & (\hat{i} \neq \hat{j}). \end{cases} \tag{30}$$

On the other hand, the trigonometric polynomial $\Pi_{\hat{i}}(x)$ of degree N has the equivalent representation [12] defined by

$$\Pi_{\hat{i}}(x) = \frac{1}{N} \sum_{k=-N/2}^{N/2-1} e^{ik(x-x_{\hat{i}})}. \tag{31}$$

Using (31), one can rewrite equation (27) as follows:

$$f_N(x) = \sum_{\hat{i}=0}^{N-1} f(x_{\hat{i}}) \frac{1}{N} \sum_{k=-N/2}^{N/2-1} e^{ik(x-x_{\hat{i}})} = \sum_{k=-N/2}^{N/2-1} \tilde{f}_k e^{ikx}, \tag{32}$$

defining

$$\tilde{f}_k = \frac{1}{N} \sum_{\hat{i}=0}^{N-1} f(x_{\hat{i}}) e^{-ikx_{\hat{i}}}, \tag{33}$$

which is in fact the discrete Fourier coefficient of $f(x)$. Thus one also can evaluate derivatives using equation (32) to obtain

$$\frac{df_N(x_{\hat{j}})}{dx} = \frac{1}{N} \sum_{k=-N/2}^{N/2-1} ik\tilde{f}_k e^{ikx}. \tag{34}$$

Note that $f_N(x_{\hat{j}}) = f(x_{\hat{j}}), \hat{j} = 0, 1, ..., N-1$, but their derivative $\frac{df_N}{dx}$ is not necessarily exact with $\frac{df}{dx}$ on the grids $x_{\hat{j}}$.

For the sake of convenience, here we use the physical space expression (29), rather than (34), for the spatial derivative D_x with respect to x in the scheme (20)–(24) using the one-dimensional derivative matrix $\hat{D}_x = [(\hat{D}_x)_{\hat{j}\hat{i}}]$ for $\hat{i}, \hat{j} = 0, ..., N_x - 1$ associated with N_x points on the interval $[0, L_x]$. Expressed as a matrix-vector product, the spatial derivative D_x reads

$$D_x \bar{E} = \begin{bmatrix} \hat{D}_x & & & \\ & \hat{D}_x & & \\ & & \ddots & \\ & & & \hat{D}_x \end{bmatrix} \bar{E}. \tag{35}$$

$\hat{D}_x$ is applied to each row $[\bar{E}_{0j}, \bar{E}_{1j}, ..., \bar{E}_{N_x-1j}]^T, j = 0, ..., N_y - 1$, in the computational grid of Figure 1. To compute the derivative with respect to y, one applies the corresponding one-dimensional $N_y \times N_y$ matrix $\hat{D}_y$ to each column $[\bar{E}_{i0}, \bar{E}_{i1}, ..., \bar{E}_{iN_y-1}]^T, i = 0, ..., N_x - 1$. This can be conveniently expressed as $D_x = I \otimes \hat{D}_x$ and $D_y = \hat{D}_y \otimes I$ using the tensor product $\otimes$ defined in [5]. Let $A = [a_{\hat{i}\hat{j}}]$ and $B = [b_{\hat{i}\hat{j}}]$ be $k \times l$ and $m \times n$ matrices, respectively. Then their tensor product is given in block matrix form as

$$A \otimes B = \begin{bmatrix} a_{11}B & a_{12}B & \cdots & a_{1l}B \\ a_{21}B & a_{22}B & \cdots & a_{2l}B \\ \vdots & \vdots & & \vdots \\ a_{k1}B & a_{k2}B & \cdots & a_{kl}B \end{bmatrix}. \tag{36}$$

3.2 Uniaxial Perpectly Matched Layer (UPML)

In the UPML region as shown in Figure 1, the fields are also planewave in nature and satisfy the Maxwell's equations. The following artificial permittivity and permeability tensors are assigned to the frequency–domain representation (1)–(5) in that region: $\breve{\epsilon} = \epsilon\breve{s}$ and $\breve{\mu}_0 = \mu_0\breve{s}$ where the diagonal tensor $\breve{s}$ is

$$\breve{s} = \begin{bmatrix} s_y s_z s_x^{-1} & 0 & 0 \\ 0 & s_x s_z s_y^{-1} & 0 \\ 0 & 0 & s_x s_y s_z^{-1} \end{bmatrix}. \tag{37}$$

This artificial tensor assignment eliminates reflections for waves propagating across the UPML boundary. The refletionless nature is retained for any given tensor elements, $s_{x,y,z}$ [27], [29]. For UPML to be an absorber, the diagonal elements of $\breve{s}$ can be chosen as

$$s_x = \mathcal{K}_x + \frac{\sigma_x}{i\omega\epsilon_0}, s_y = \mathcal{K}_y + \frac{\sigma_y}{i\omega\epsilon_0}, \text{ and } s_z = \mathcal{K}_z + \frac{\sigma_z}{i\omega\epsilon_0}, \tag{38}$$

where the constants $\mathcal{K}_{x,y,z}$ are real. The effect from the abrupt change of UPML conductivity, $\sigma_{x,y,z}$, from non-UPML to UPML region can be reduced by smoothly increasing UPML conductivity. We choose polynomial gratings as follows ; for example, assuming $x = x_0$ at the interface of non-UPML and UPML region and considering s_x for $x - x_0 \leq 0$,

$$\sigma_x = \left(\frac{x - x_0}{d}\right)^m \sigma'_{x,\max}, \text{ and } \sigma'_{x,\max} = -\frac{(m+1)\ln[R(0)]}{2\eta d}. \tag{39}$$

where $\eta = \sqrt{\mu_0/\epsilon}$ and d is the thickness of PML slab. We use empirically optimized UPML parameters. That is $m = 1$, $\mathcal{K}_{x,y,z} = 1$, and $R(0) = 10^{-12}$. UPML tensor elements are designed to act on a specific wave propagation, corresponding to a subscript propagation component; for example, s_x acts on wave propagating in x–direction. For two–dimensional computations on x–y plane, we set $s_y = s_z = 1$ for x–directed domain boundary and $s_x = s_z = 1$ for y–directed domain boundary. Then, the frequency domain representation of the UPML tensor can be incorporated with PSTD updating scheme through the constitutive relation [29].

3.3 Computations

We obtained computational results using the Fourier pseudospectral time-domain (PSTD) method (20)–(24) with the UPML formulations (37)–(39) in the absorbing layer. Specifically, we examined snapshots of the field components E_x, E_y in a local domain $\Omega = [640, 896] \times [128, 384]\,\text{nm}^2$, the region within the dotted line in Figure 1, and frequency-domain field distributions $\tilde{E}$, $\tilde{H}$ at a frequency ω_0 defined in Ω as follows :

$$\tilde{E}(x, y, \omega_0) = \int_0^\infty e^{i\omega_0 t} E(x, y, t)dt, \tag{40}$$

$$\tilde{H}(x, y, \omega_0) = \int_0^\infty e^{i\omega_0 t} E(x, y, t)dt. \tag{41}$$

For snapshots, we used modulated Blackman-Harris pulses [9] covering the range of frequencies $[\frac{c}{\lambda_0} - a, \frac{c}{\lambda_0} + a]$ Hz, where a =1.800e14, λ_0 =340 nm and $c = \frac{1}{\sqrt{\mu_0\epsilon_0}}$.

To ensure the numerical stability in time, we used an allowable time step as in [9], [20], [24],

$$\Delta t < \frac{2\sqrt{\epsilon_{\min}/\epsilon_0}}{\pi c\sqrt{1/\Delta x^2 + 1/\Delta y^2}}, \tag{42}$$

where $\epsilon_{\min} = \min\{\epsilon_0, \epsilon_0\epsilon_\infty\}$. However, a rigorous stability analysis for our problem is not provided in this paper.

Note that, because of a hard line source used in the simulation, the pulse width and the final time must be chosen so that retroreflected waves from the line-source cannot get into the local domain Ω. The snapshots

for the field components E_x and E_y at time 11.48e-15 sec with Δt =1.3514e-18 required 8,495 iterations in time and a total CPU time of 7669.9 sec for $\Delta x = \Delta y = 1$ nm (see Figures 8–11 at the end of the paper).

For frequency-domain simulations, we used the range of frequencies $[\frac{c}{\lambda_0} - b, \frac{c}{\lambda_0} + b]$ Hz, where b =7.365e14, λ_0 =340 nm for the source pulse. The pulse width should be short enough to avoid retroreflected waves from the source getting into the local domain Ω, and the total physical simulation time must be chosen so that the fields go to zero at the end of simulation, avoiding a time-window effect. We obtained the distributions of the time-averaged electric field by computing the magnitude of the equation (40). We used the compact line source [21] at the sinusoidal frequency $w_0 = \frac{2\pi c}{\lambda_0}$ Hz. The same size of Δt required 22,200 iterations in time and a total CPU time of 7893.9 sec for finer grid sizes $\Delta x = \Delta y = 0.5$ nm (see Figures 12–14 at the end of the paper).

However, we observe nonphysical oscillations in the PSTD solutions. In our problem configuration, the solution is piecewise smooth as a result of the discontinuity in the dielectric function along the interface of the cylinder. Hence, we cannot obtain an accurate approximate solution with the standard Fourier pseudospectral method, although that is a good method for analytic and periodic functions. In the next sections, we introduce a cost-effective reconstruction technique as a postprocessing method and use it to increase the order of accuracy for our PSTD solutions by reducing the nonphysical oscillations.

4 Gegenbauer Reconstructions in Finite Spaces

Although the results by Fourier pseudospectral time-domain simulations are obscured by oscillations arising from the Gibbs phenomenon, one can recover accurate reconstructions by using either Fourier-Padé approximations [26] or Gegenbauer polynomials [15], [23].

Here, we consider Gegenbauer reconstructions. This method requires a priori knowledge of the location of the discontinuity. In the present application, the discontinuity location, which arises from the jump in dielectric function, is specified as part of the problem definition, and Gegenbauer reconstruction is therefore appropriate.

4.1 Gibbs Phenomenon

We briefly revisit the prototype problem of Gibbs oscillation. Consider a nonperiodic analytic function $f(x)$ in $[-1, 1]$. Now, assume that the point values $f(x_j)$, where $x_j = 2j/N, j = 0, ..., N-1$, are known but the function $f(x)$ is not. This is equivalent to knowing the first N discrete Fourier coefficients $\tilde{f}_k$, $-N/2 \leq k \leq N/2 - 1$, of the function $f(x)$ defined by

$$\tilde{f}_k = \sum_{j=0}^{N-1} f(x_j) e^{-i\pi k x_j}. \tag{43}$$

Then the classical Fourier sum

$$f_N(x) = \sum_{k=-N/2}^{N/2-1} \tilde{f}_k e^{i\pi k x} \tag{44}$$

reconstructs the point values everywhere in $-1 \leq x \leq 1$.

The finite Fourier expansion converges exponentially as N increases when the approximated function is analytic (i.e., inifinitely smooth) and periodic [13]. If $f(x)$ is either discontinuous or nonperiodic, however, then $f_N(x)$ is not a good approximation to $f(x)$. Away from the discontinuity or the boundary, the convergence is only $O(\frac{1}{N})$, and there is an overshoot close to the discontinuity or the boundary that does not diminish with increasing N [13]; this is referred to as the Gibbs phenomenon [11]. The phenomenon manifests itself in many situations, including the problem we present in this paper.

4.2 Review of Gegenbauer Approximations

Gottlieb and Shu showed that, knowing the first N Fourier coefficients, one can reconstruct a *rapidly converging* series based on the expansions in Gegenbauer polynomials [15]. The point values of $f(x)$ everywhere in $-1 \leq x \leq 1$ can be recovered with exponential accuracy in the maximum norm up to the discontinuity or the boundary.

The Gegenbauer series for the function $f(x)$, based on the Gegenbauer polynomials $C_n^\alpha(x)$, which are orthogonal over the range $x \in [-1, 1]$ with the weight function $(1-x^2)^{\alpha-\frac{1}{2}}$ for any constant $\alpha \geq 0$, is defined by

$$f(x) = \sum_{n=0}^{\infty} \hat{b}_n^\alpha C_n^\alpha(x), \tag{45}$$

where the continuous Gegenbauer coefficient is defined by

$$\hat{b}_n^\alpha = \frac{1}{h_n^\alpha} \int_{-1}^{1} (1-x^2)^{\alpha-\frac{1}{2}} C_n^\alpha(x) f(x) dx, \tag{46}$$

with the normalization constant

$$h_n^\alpha = \pi^{\frac{1}{2}} C_n^\alpha(1) \frac{\Gamma(\alpha+\frac{1}{2})}{\Gamma(\alpha)(n+\alpha)} \quad \text{and} \quad C_n^\alpha(1) = \frac{\Gamma(n+2\alpha)}{n!\Gamma(2\alpha)}. \tag{47}$$

The Gegenbauer polynomials can be expressed by Rodrigues's formula [1], and more conventionally they can be computed by the following recurrence formula [1]:

$$nC_n^\alpha(x) = 2(n+\alpha-1)xC_{n-1}^\alpha(x) - (n+2\alpha-2)C_{n-2}^\alpha(x). \tag{48}$$

They achieve their maximum at the boundary

$$|C_n^\alpha(x)| \leq |C_n^\alpha(1)|, \quad -1 \leq x \leq 1. \tag{49}$$

For large α and n, h_n^α and $C_n^\alpha(1)$ are almost of the same size, which is proven by using Stirling's formula [1], [14]. In Figure 2, Gegenbauer polynomials of degree $n = 5$ are shown for different α. As α increases, the amplitude of $C_5^\alpha(x)$ dramatically increases at the boundary. On the other hand, the weight functions rapidly approach zero near the boundary as α increases. The convergence rate of the infinite series depends on the rate of decay in the magnitude of the coefficients. A rigorous proof of the exponential convergence of the Gegenbauer series to an analytic function $f(x)$ is shown in [14], [15].

Note that more commonly used Chebyshev and Legendre polynomials are important subclasses of the Gegenbauer polynomials with the relations

$$T_n(x) = n \lim_{\alpha \to 0} \Gamma(2\alpha) C_n^\alpha(x), \quad L_n(x) = C_n^{\frac{1}{2}}(x), \tag{50}$$

where $T_n(x)$ and $L_n(x)$ represent Chebyshev and Legendre polynomials of degree n, respectively. Figure 2 shows some profiles of them for degree $n = 1, 2, ..., 5$. They are obtained by using a cost-effective version for computing the Gegenbauer polynomials; this method is discussed in Section 3 and 4. For computation of the Chebyshev polynomials, following the relation in (50), α is chosen as 1.0e-11 for the limit relation, which gives polynomial accuracy to 7 digits.

The sum of the first $M+1$ terms of the Gegenbauer expansion in (45), denoted by

$$g_M^\alpha(x) = \sum_{n=0}^{M} \hat{b}_n^\alpha C_n^\alpha(x), \tag{51}$$

converges exponentially to an analytic function $f(x)$ in $[-1, 1]$. In practice, however, the continuous coefficients $\hat{b}_n^\alpha$ must be computed and they are computed in a discrete sense. Assume that we are given only

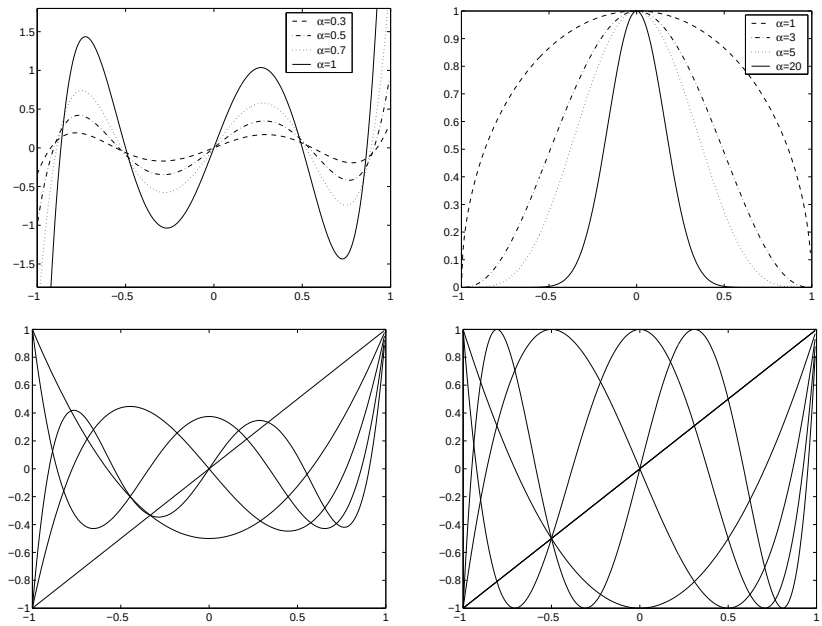

Figure 2: First row: From left, Gegenbauer polynomials $C_5^\alpha(x)$ and weight functions $(1-x^2)^{\alpha-\frac{1}{2}}$ for various α. Second row: Subclasses of Gegenbauer polynomials, from left, Legendre polynomials $L_n(x)$ and Chebyshev polynomials $T_n(x)$ for $n = 1, 2, ..., 5$.

an approximation of $f(x)$, the Fourier pseudospectral data, in our problem. It was shown that the Fourier finite expansion (44) can be used to approximate $\hat{b}_n^\alpha$. Now we define the discrete Gegenbauer coefficients b_n^α, instead of the continuous Gegenbauer coefficients $\hat{b}_n^\alpha$, by substituting $f(x)$ by $f_N(x)$ in (46). Then the discrete Gegenbauer finite expansion is expressed as

$$g_{M,N}^\alpha(x) = \sum_{n=0}^{M} b_n^\alpha C_n^\alpha(x), \tag{52}$$

where the discrete Gegenbauer coefficients are defined by using $f_N(x)$ as follows:

$$b_n^\alpha = \frac{1}{h_n^\alpha} \int_{-1}^{1} (1-x^2)^{\alpha-\frac{1}{2}} C_n^\alpha(x) f_N(x) dx. \tag{53}$$

In fact, one can represent the discrete Gegenbauer coefficient in terms of the discrete Fourier coefficients. Plugging (44) into (53), one obtains the following

$$b_n^\alpha = \sum_{k=-\frac{N}{2}}^{\frac{N}{2}-1} \tilde{f}_k \left(\frac{1}{h_n^\alpha} \int_{-1}^{1} (1-x^2)^{\alpha-\frac{1}{2}} C_n^\alpha(x) e^{i\pi kx} dx \right), \tag{54}$$

where the integration part has an explicit form [3] for $k \neq 0$ as

$$\frac{1}{h_n^\alpha} \int_{-1}^{1} (1-x^2)^{\alpha-\frac{1}{2}} C_n^\alpha(x) e^{i\pi kx} dx = \Gamma(\alpha)(\frac{2}{k\pi})^\alpha i^n (n+\alpha) J_{n+\alpha}(k\pi), \tag{55}$$

where $\Gamma(x)$ is the gamma function and $J_n(x)$ is the Bessel function of first kind. For $k = 0$, one uses the

orthogonal property of the Gegenbauer polynomials. Thus we have

$$b_n^\alpha = \tilde{f}_0 \delta_{0n} + \sum_{k=-\frac{N}{2}, k\neq 0}^{\frac{N}{2}-1} \tilde{f}_k \Gamma(\alpha)(\frac{2}{k\pi})^\alpha i^n (n+\alpha) J_{n+\alpha}(k\pi). \tag{56}$$

There are two contributing errors to the discrete Gegenbauer finite approximation $g_{M,N}^\alpha$, the truncation error and the regularization error. The truncation error results from the difference between the $(M+1)$ term Gegenbauer expansion g_M^α of the function $f(x)$, and the approximation $g_{M,N}^\alpha$ through replacing the function $f(x)$ by the truncated Fourier expansion $f_N(x)$ in the coefficients. The regularization error is introduced by the truncated Gegenbauer expansion g_M^α to the function $f(x)$. Thus one can decompose the error of the approximation $g_{M,N}^\alpha$ to $f(x)$ as the following and make it exponentially small

$$\|f - g_{M,N}^\alpha\| \leq \|f - g_M^\alpha\| + \|g_M^\alpha - g_{M,N}^\alpha\|, \tag{57}$$

by showing the two terms on the right-hand side to be exponentially small, separately. Define the *truncation error* as follows:

$$\|g_M^\alpha - g_{M,N}^\alpha\| = \max_{-1\leq x\leq 1} |\sum_{n=0}^{M} (\hat{b}_n^\alpha - b_n^\alpha) C_n^\alpha(x)|, \tag{58}$$

which is exponentially small in maximum norm over $[-1,1]$ if *both α and M grow linearly with N* [14], [15]. Then the *regularization error* is defined by

$$\|f - g_M^\alpha\| = \max_{-1\leq x\leq 1} |f(x) - \sum_{n=0}^{M} \hat{b}_n^\alpha C_n^\alpha(x)|, \tag{59}$$

which is again exponentially small for $\alpha = \gamma M$ with any positive constant γ [14], [15].

Note that, for a fixed α and N, the approximation $g_{M,N}^\alpha$, of course, converges to $f_N(x)$ as M increases to infinity, which is not the desired result. Rather, one must consider simultaneous variations in M, α and N to achieve the exponential convergence. In applications, the number of Fourier coefficients, N, is fixed. Thus α and M are free parameters to be chosen depending on N and also on the size of each subdomain. The optimum relation between the parametes and other factors has been analyzed analytically in [15]. In real computation, however, it requires adjustment. Few computational studies of optimizing parameters have been done so far. In this paper, we show successful computational results obtained by appropriate parameters chosen from many numerical experiments. These results are discussed in Section 5.

The suggested procedure to obtain the discrete Gegenbauer finite expansion $g_{M,N}^\alpha$ generally consists of the following steps:

Step 1. Compute the first $M+1$ discrete Gegenbauer coefficients b_n^α in (54) by using $f_N(x)$.

Step 2. Construct the series (52) cost-effectively by expressing the Gegenbauer polynomials in terms of trigonometric functions.

In the next sections, we first discuss the detailed procedure for single-domain and multidomain reconstruction in one dimension and then extend the procedure to two dimensions.

4.3 Single-Domain Reconstruction

Here, we focus on a cost-effective Gegenbauer reconstruction to compute $g_{M,N}^\alpha$ for a single domain on $[-1,1]$. Let us define the following notation for formula (55):

$$\begin{aligned} \text{For } k\neq 0, \quad B_{n,k} &= \Gamma(\alpha)(\frac{2}{k\pi})^\alpha i^n (n+\alpha) J_{n+\alpha}(k\pi), \\ \text{For } k = 0, \quad B_{n,k} &= \delta_{nk}. \end{aligned} \tag{60}$$

Then the discrete Gegenbauer coefficients b_n^α in (56) can be written in matrix form as

$$\begin{bmatrix} b_0^\alpha \\ b_1^\alpha \\ \cdot \\ \cdot \\ b_M^\alpha \end{bmatrix} = \begin{bmatrix} B_{0,-\frac{N}{2}} & B_{0,-\frac{N}{2}+1} & \cdots & B_{0,\frac{N}{2}-1} \\ B_{1,-\frac{N}{2}} & B_{1,-\frac{N}{2}+1} & \cdots & B_{1,\frac{N}{2}-1} \\ \cdot & \cdot & \cdots & \cdot \\ \cdot & \cdot & \cdots & \cdot \\ B_{M,-\frac{N}{2}} & B_{M,-\frac{N}{2}} & \cdots & B_{M,\frac{N}{2}-1} \end{bmatrix} \begin{bmatrix} \tilde{f}_{-\frac{N}{2}} \\ \tilde{f}_{-\frac{N}{2}+1} \\ \cdot \\ \cdot \\ \tilde{f}_{\frac{N}{2}-1} \end{bmatrix}.$$

Applying the even and odd property of the Bessel function, we have $B_{n,k} = \overline{B_{n,-k}}$. For a real function $f(x)$, the Fourier coefficients are $\tilde{f}_k = \overline{\tilde{f}_{-k}}$. Thus we have

$$\begin{aligned} b_n^\alpha &= B_{n,-\frac{N}{2}}\tilde{f}_{-\frac{N}{2}} + \sum_{k=-(\frac{N}{2}-1)}^{-1} B_{n,k}\tilde{f}_k + +B_{0,0}\tilde{f}_0 + \sum_{k=1}^{\frac{N}{2}-1} B_{n,k}\tilde{f}_k \\ &= B_{n,-\frac{N}{2}}\tilde{f}_{-\frac{N}{2}} + B_{0,0}\tilde{f}_0 + \sum_{k=1}^{\frac{N}{2}-1} (B_{n,k}\tilde{f}_k + \overline{B_{n,k}\tilde{f}_k}). \end{aligned} \tag{61}$$

By taking the conjugate of $(N/2-1)$ terms of $B_{n,k}\tilde{f}_k$, we can now reduce the computational cost for computing the Gegenbauer coefficients from $O(N)$ to $O(N/2)$.

Next, following the procedure introduced in [23], we take the explicit form of the Gegenbauer polynomials expanded by the trigonometric polynomials, instead of using the conventional recurrence formula [3]: for $x = \cos\theta \in [-1, 1]$ with $\theta \in [-\pi, \pi]$,

$$C_n^\alpha(\cos\theta) = \sum_{m=0}^{n} a_{m,n}^\alpha \cos(n-2m)\theta, \tag{62}$$

where

$$a_{m,n}^\alpha = \frac{\Gamma(\alpha+m)\Gamma(\alpha+n-m)}{m!(n-m)!\Gamma^2(\alpha)}. \tag{63}$$

Let us consider a set of grids x_i, $i = 0, ..., N-1$. Then the approximate Gegenbauer expansion on grids x_i is

$$\begin{aligned} g_{M,N}^\alpha(x_i) &= \sum_{n=0}^{M} b_n^\alpha C_n^\alpha(\cos x_i) \\ &= \sum_{n=0}^{M} b_n^\alpha \left(\sum_{m=0}^{n} a_{m,n} \cos[(n-2m)(\cos^{-1} x_i)] \right). \end{aligned} \tag{64}$$

Let $T_{i,m} = \cos(m\theta_i)$ for $\theta_i = \cos^{-1} x_i$ and $\mathbf{g_i} = g_{M,N}^\alpha(x_i)$. Assuming that M is even for the sake of simplicity, we can express the Gegenbauer reconstruction on the grids x_i in matrix form as follows:

$$\begin{bmatrix} \mathbf{g}_0 \\ \mathbf{g}_1 \\ \cdot \\ \cdot \\ \cdot \\ \mathbf{g}_{N-1} \end{bmatrix} = \begin{bmatrix} T_{0,0} & T_{0,1} & \cdots & T_{0,M} \\ T_{1,0} & T_{1,1} & \cdots & T_{1,M} \\ \cdot & \cdot & \cdots & \cdot \\ \cdot & \cdot & \cdots & \cdot \\ \cdot & \cdot & \cdots & \cdot \\ T_{N-1,0} & T_{N-1,1} & \cdots & T_{N-1,M} \end{bmatrix} \begin{bmatrix} a_{00}^\alpha & 0 & a_{12}^\alpha & 0 & \cdots & a_{\frac{M}{2},M}^\alpha \\ 0 & 2a_{01}^\alpha & 0 & 2a_{13}^\alpha & \cdots & 0 \\ 0 & 0 & 2a_{02}^\alpha & 0 & \cdots & 0 \\ \cdot & \cdot & 0 & \cdot & \cdots & 2a_{1M}^\alpha \\ \cdot & \cdot & \cdot & 0 & \cdots & 0 \\ 0 & 0 & 0 & 0 & 0 & 2a_{0M}^\alpha \end{bmatrix} \begin{bmatrix} b_0^\alpha \\ b_1^\alpha \\ \cdot \\ \cdot \\ \cdot \\ b_M^\alpha \end{bmatrix}.$$

To discuss the computational cost, we denote the first $N \times (M+1)$ matrix in the right side of the above equation by $\mathbf{T}$ and the second $(M+1) \times (M+1)$ matrix by $\mathbf{A}$, that is,

$$\mathbf{g} = \mathbf{TAb}, \tag{65}$$

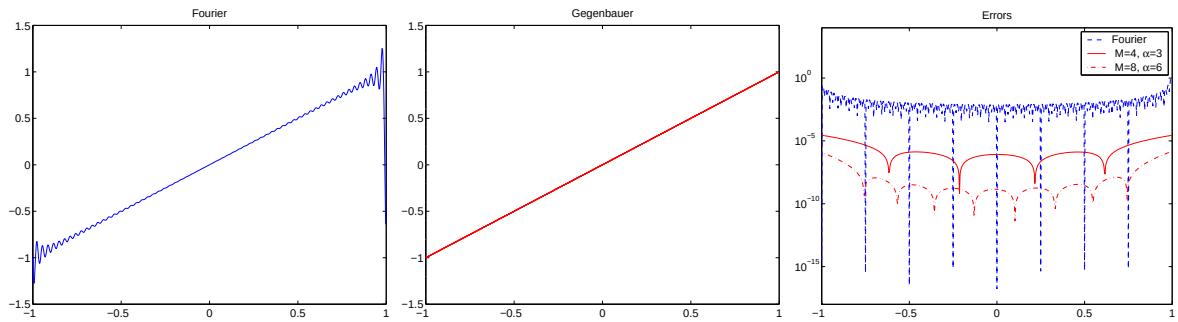

Figure 3: From the left: Fourier approximation, its Gegenbauer reconstruction, and pointwise errors. Reconstruction CPU time = 0.22 sec and 0.42 sec for $M = 4, \alpha = 3$ and $M = 8, \alpha = 6$, respectively, on an AMD Athlon of 1 GHz.

where $\mathbf{g} = [\mathbf{g_0}, \mathbf{g_1}, ...\mathbf{g_{N-1}}]^{\mathbf{T}}$ and $\mathbf{b} = [b_0^\alpha, b_1^\alpha, ..., b_M^\alpha]^T$. The number of operations for the matrix-vector multiplication $\mathbf{Ab}$ is $\frac{(M+2)(M+4)}{4}$, and the multiplication with $\mathbf{T}$ is $N(M+1)$. Then, for $M = \beta N$ $(0 < \beta < 1)$ (i.e., proportional to N), the total cost is $O(\frac{1}{4}\beta(\beta+4)N^2)$. On the other hand, the conventional recurrence formula (48) costs $O(3\beta N^2)$. Since $\frac{\beta+4}{4} \approx 1$, the fast version reduces the computational cost by one-third.

In summary, the reconstruction procedure comprises the following general steps:

Step 1. Compute the first $M+1$ discrete Gegenbauer coefficients (61).

Step 2. Construct the Gegenbauer finite sum on grids following (65).

Example 1. We apply the reconstruction technique to Fourier pseudospectral data of a nonperiodic function $f(x) = x$ on $[-1, 1]$, assuming that we are given $N = 128$ discrete Fourier coefficients, as defined in (43), on the grids $x_i = -1 + 2i/N, i = 0, ..., N-1$. Figure 3 shows the Fourier approximation with $N = 128$ modes, its reconstructed results, and their pointwise errors. Since the function $f(x)$ is nonperiodic, the standard Fourier method gives only $O(\frac{1}{N})$ away from the boundary and $O(1)$ convergence at the boundary, and oscillations are severe near the boundary. Since $f_N(x_i)$ is exact with $f(x_i)$ on grids x_i, the point values are evaluated on $y_i = -1 + i/N, i = 0, ..., 2N-1$ in order to see the oscillations and their resolution clearly. After reconstruction with the parameters $m = 4, \alpha = 3$, the original function $f(x) = x$ is recovered successfully. As the parameters increase to $m = 8, \alpha = 6$, the errors drop exponentially up to the boundary. Reconstruction CPU times are provided.

4.4 Multidomain Reconstruction

Consider a piecewise analytic function $f(x)$ that is integrable in $[0, L]$. Suppose that $f(x)$ has known discontinuities at $x = d_0$ and $x = d_1$ in $[0, L]$. Then we divide the global domain into three subdomains, denoted by $\Omega_1 = [0, d_0]$, $\Omega_2 = [d_0, d_1]$, and $\Omega_2 = [d_1, L]$, and carry out the Gegenbauer reconstruction in each subdomain. First, we define a set of grids in the global domain defined by $x_j = \frac{Lj}{N}$, $j = 0, 1, ..., N-1$ and assume that the point values $f(x_j)$ $(j = 0, 1, ..., N-1)$ are given. Then we obtain the Fourier coefficients $\tilde{f}_k(-\frac{N}{2} \le k \le \frac{N}{2} - 1)$ by applying a discrete fast Fourier transform, so that the classical Fourier finite sum everywhere in $[0, L]$ is defined by

$$f_N(x) = \sum_{k=-\frac{N}{2}}^{\frac{N}{2}-1} \tilde{f}_k e^{i\frac{2\pi k}{L}x}. \tag{66}$$

Let us denote a subdomain by $\Omega_s = [a,b]$ and define a local variable, for $\xi \in [-1,1]$, $x^s = \frac{(b-a)}{2}\xi + \frac{(b+a)}{2}$. Let $\epsilon = \frac{b-a}{L}$ and $\delta = \frac{b+a}{L}$. The Fourier finite sum using the variable ξ is

$$f_N(x(\xi)) = \sum_{k=-\frac{N}{2}}^{\frac{N}{2}-1} \tilde{f}_k e^{i\pi k(\epsilon\xi+\delta)}. \tag{67}$$

Now we define the Gegenbauer coefficients in each subdomain:

$$b_n^{\Omega_s} = \frac{1}{h_n^\alpha}\int_{-1}^{1}(1-\xi^2)^{\alpha-\frac{1}{2}}C_n^\alpha(\xi)f_N(x(\xi))d\xi. \tag{68}$$

Then plugging (67) into (68) and using the explicit formula (55) for the integration part, we denote

$$\begin{aligned}
\text{For } k \neq 0, \quad B_{n,k}^{\Omega^s} &= \frac{e^{i\pi k\delta}}{h_n^\alpha}\int_{-1}^{1}(1-\xi^2)^{\alpha-\frac{1}{2}}C_n^\alpha(\xi)e^{i\pi k\epsilon\xi}d\xi \\
&= e^{i\pi k\delta}\Gamma(\alpha)(\frac{2}{k\pi\epsilon})^\alpha i^n(n+\alpha)J_{n+\alpha}(k\epsilon\pi), \\
\text{For } k = 0, \quad B_{n,k}^{\Omega^s} &= \delta_{nk}.
\end{aligned} \tag{69}$$

Then, the local Gegenbauer coefficients are expressed in a matrix form:

$$\begin{bmatrix} b_0^{\Omega_s} \\ b_1^{\Omega_s} \\ \cdot \\ \cdot \\ b_M^{\Omega_s} \end{bmatrix} = \begin{bmatrix} B_{0,-\frac{N}{2}}^{\Omega_s} & B_{0,-\frac{N}{2}+1}^{\Omega_s} & \cdots & B_{0,\frac{N}{2}-1}^{\Omega_s} \\ B_{1,-\frac{N}{2}}^{\Omega_s} & B_{1,-\frac{N}{2}+1}^{\Omega_s} & \cdots & B_{1,\frac{N}{2}-1}^{\Omega_s} \\ \cdot & \cdot & \cdots & \cdot \\ \cdot & \cdot & \cdots & \cdot \\ B_{M,-\frac{N}{2}}^{\Omega_s} & B_{M,-\frac{N}{2}}^{\Omega_s} & \cdots & B_{M,\frac{N}{2}-1}^{\Omega_s} \end{bmatrix} \begin{bmatrix} \tilde{f}_{\frac{-N}{2}} \\ \tilde{f}_{\frac{-N}{2}+1} \\ \cdot \\ \cdot \\ \tilde{f}_{\frac{N}{2}-1} \end{bmatrix}.$$

Next, we evaluate the point values in each subdomain as follows. Let $\mathbf{x}^s = \{x_i^s, ..., x_j^s\}$ be a subset of $\{x_j\}_{j=0}^{N-1}$, which is in Ω_s. Define $T_{i,m}^s = \cos[m(\cos^{-1}\xi_i)]$ for $\xi_i = \frac{2}{b-a}x_i^s - \frac{b+a}{b-a}$. Note that the Gegenbauer coefficients are newly computed in each subdomain and the reconstructed point values, denoted by $\mathbf{g}_i^{\Omega_s}$, on grid set $\mathbf{x}^s$ in each subdomain are obtained by

$$\begin{bmatrix} \mathbf{g}_i^{\Omega_s} \\ \cdot \\ \cdot \\ \cdot \\ \cdot \\ \cdot \\ \mathbf{g}_j^{\Omega_s} \end{bmatrix} = \begin{bmatrix} T_{i,0}^s & T_{i,1}^s & \cdots & T_{i,M}^s \\ \cdot & \cdot & \cdots & \cdot \\ \cdot & \cdot & \cdots & \cdot \\ \cdot & \cdot & \cdots & \cdot \\ \cdot & \cdot & \cdots & \cdot \\ T_{j,0}^s & T_{j,1}^s & \cdots & T_{j,M}^s \end{bmatrix} \begin{bmatrix} a_{00} & 0 & a_{12} & 0 & \cdots & a_{\frac{M}{2},M} \\ 0 & 2a_{01} & 0 & 2a_{13} & \cdots & 0 \\ 0 & 0 & 2a_{02} & 0 & \cdots & 0 \\ \cdot & \cdot & 0 & \cdot & \cdots & 2a_{1M} \\ \cdot & \cdot & \cdot & 0 & \cdots & 0 \\ 0 & 0 & 0 & 0 & 0 & 2a_{0M} \end{bmatrix} \begin{bmatrix} b_0^{\Omega_s} \\ b_1^{\Omega_s} \\ \cdot \\ \cdot \\ \cdot \\ b_M^{\Omega_s} \end{bmatrix}.$$

Let N^s be the number of the elements in $\mathbf{x}^s$ and D the number of discontinuities. Then the first $N^s \times (M+1)$ matrix in the right-hand side of the equation above is denoted by $\mathbf{T}^s$ and the second $(M+1)\times(M+1)$ matrix by $\mathbf{A}^s$. Then

$$\mathbf{g^s} = \mathbf{T^s A^s b^s}, \tag{70}$$

where $\mathbf{g}^s = [g_i^{\Omega_s}, ...g_j^{\Omega_s}]^T$ and $\mathbf{b}^s = [b_0^{\Omega_s}, b_1^{\Omega_s}, ..., b_M^{\Omega_s}]^T$. The number of operations for the matrix-vector multiplication $\mathbf{A}^s\mathbf{b}^s$ is $\frac{(M+2)(M+4)}{4}$. However, one has to compute this procedure for each subdomain, so the amount of work for this procedure is $\mathcal{M}^S = \sum_{s=1}^{S}\frac{(M^s+2)(M^s+4)}{4}$ where $S(\geq D)$ stands for the number of subdomains. After multiplication with $\mathbf{T^s}$, the total amount of work is $\frac{N^s(M^s+2)(M^s+4)}{4}$ in each subdomain. Thus, denoted by $M_{\max} = \max\{M^s\}$, for $M_{\max} = \beta N$, $(0 < \beta < 1)$ (i.e., proportional to N), the total cost is $O(\frac{1}{4}\beta(S\beta+4)N^2)$. On the other hand, the conventional recurrence formula costs $O(3S\beta N^2)$.

In summary, the reconstruction procedure for multidomain case is as follows :

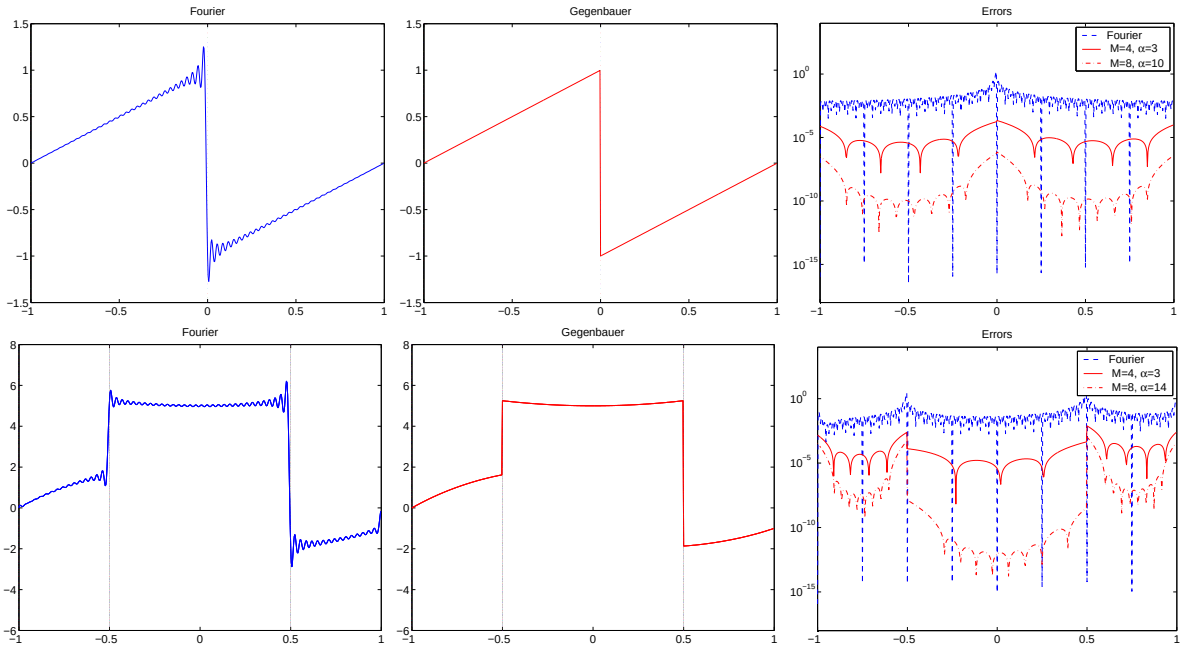

Figure 4: From the left columns: Fourier approximations, their Gegenbauer reconstructions, and pointwise errors. Reconstruction CPU time: 0.47 sec ($M = 4, \alpha = 3$) and 0.90 sec ($M = 8, \alpha = 10$) for $f_1(x)$, and 0.72 sec ($M = 4, \alpha = 3$) and 1.38 sec ($M = 8, \alpha = 16$) for $f_2(x)$ on an AMD Athlon of 1 GHz.

Step 1. Compute the first $M + 1$ discrete Gegenbauer coefficients (68) in a subdomain.
Step 2. Construct the Gegenbauer finite sum (70) on the grids in the subdomain.
Step 3. Repeat Step 1 and Step 2 in the remaining subdomains, separately.

Example 2. Consider the following discontinuous functions, and assume that we are given only $N = 128$ discrete Fourier coefficients, as defined in (43), for each function:

$$f_1(x) = \begin{cases} x + 1 (-1 \le x \le 0) \\ x - 1 (0 \le x \le 1) \end{cases} \quad \text{and} \quad f_2(x) = \begin{cases} x^3 - x^2 + 2 (-1 \le x \le -\frac{1}{2}) \\ x^2 + 5 (-\frac{1}{2} \le x \le \frac{1}{2}) \\ x^3 - 2 (\frac{1}{2} \le x \le 1). \end{cases} \tag{71}$$

Figure 4 shows the Fourier approximations with $N = 128$, their reconstructed results and the pointwise errors for the functions. For discontinuous functions, the standard Fourier approximation gives only $O(\frac{1}{N})$ convergence away from the discontinuities and $O(1)$ convergence near the discontinuities, as shown in the error plot. Reconstructions are carried out for the function $f_1(x)$ with two subdomains and for the function $f_2(x)$ with three subdomains. For the reconstructed ones with increasing parameters, the errors drop exponentially up to discontinuities.

Example 3. Consider the following piecewise analytic function $f_3(x)$, and assume that we are given only $N = 256$ discrete Fourier coefficients:

$$f_3(x) = \begin{cases} (x + 0.43)^2 (-1 \le x < -0.43) \\ 40(x + 0.43)^2 (-0.43 \le x < -0.33) \\ 10(x + 0.23)^2 (-0.33 \le x < -0.23) \\ -5(x^2 - 0.0529)(-0.23 \le x < 0.23) \\ -5(x - 0.23)^2 (0.23 \le x < 0.33) \\ -30(x - 0.43)^2 (0.33 \le x < 0.43) \\ 0.5(x - 0.43)^2 (0.43 \le x \le 1). \end{cases} \tag{72}$$

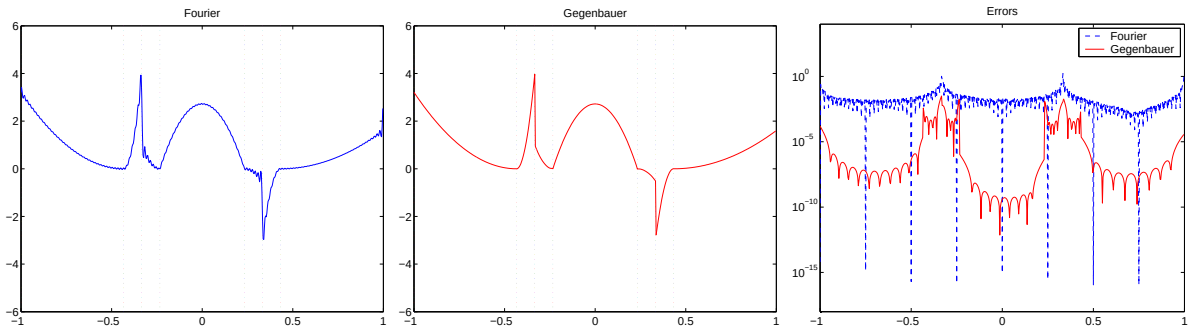

Figure 5: From the left: Fourier approximation, its Gegenbauer reconstruction, and pointwise errors. Parameters for Gegenbauer reconstruction are chosen as $M = 10, 4, 5, 8, 5, 4, 8$ and $\alpha = 6, 4, 5, 8, 5, 4, 6$ for 7 subdomains. Reconstruction CPU time: 3.83 sec on an AMD Athlon of 1 GHz.

Figure 5 shows the Fourier approximation with $N = 256$, its reconstructed result and the pointwise errors. Reconstructions are carried out with 7 subdomains whose interfaces are indicated by the vertical dotted lines. Parameters are chosen as $M = 10, 4, 5, 8, 5, 4, 8$ and $\alpha = 6, 4, 5, 8, 5, 4, 6$ in the order from the left subdomain. The error for the reconstructed one drops up to discontinuities and kinks compared to the Fourier result.

4.5 Reconstruction Time

Since the reconstruction requires to compute the Gegenbauer coefficients in each subdomain, we first examine the computation time to obtain a set of the $(M+1)$ Gegenbauer coefficients with N Fourier data in a single subdomain. Figure 6 shows the cases of $M = 1, ..., 20$ for $N = 32, 64, 128, 256$ for a fixed $\alpha = 1$. For different α, the CPU time is scaled by a constant number. One can estimate the total reconstruction time. If the CPU time to perform a one subdomain reconstruction is $c^s_{M,N}$, then the total cost to perform this reconstruction in domain is $\sum_s c^s_{M,N}$ which is in fact proportional to the time obtained by multiplying the number of the subdomains to the maximum of the subdomain reconstruction CPU times: i.e., cS, $c = \max_s\{c^s_{M,N}\}$.

5 Two-Dimensional Reconstruction

In this section, we extend the use of the cost-effective version of the Gegenbauer reconstruction technique to two-dimensional problems.

5.1 Global Domain $[-1, 1]^2$

The Gegenbauer finite sum in two dimensions has the following form. For $x = \cos\theta, y = \cos\eta$ in a domain $\Omega = [-1, 1]^2$, denoting $\alpha = (\alpha_x, \alpha_y)$ and $M = (M_x, M_y)$, we have

$$g^\alpha_{M,N}(x, y) = \sum_{n=0}^{M_x}\sum_{l=0}^{M_y} b^\alpha_{n,l} C^{\alpha_x}_n(x) C^{\alpha_y}_l(y), \tag{73}$$

where

$$C^\alpha_n(\cos\theta) = \sum_{m=0}^{n} a^\alpha_{m,n}\cos(n-2m)\theta, \tag{74}$$

and

$$a^\alpha_{m,n} = \frac{\Gamma(\alpha+m)\Gamma(\alpha+n-m)}{m!(n-m)!\Gamma^2(\alpha)}, \tag{75}$$

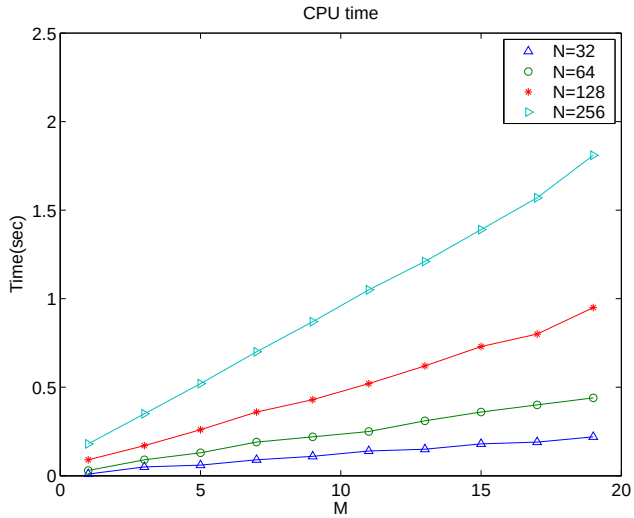

Figure 6: CPU time for computing the $(M+1)$ Gegenbauer coefficients with the parameters $M = 1, ..., 20$, $N = 32, 64, 128, 256$ and $\alpha = 1$ on an AMD Athlon of 1 GHz.

where Γ is the gamma function. The coefficients $b^{\alpha}_{n,l}$ for the Gegenbauer finite sum in two dimensions are defined by

$$b^{\alpha}_{n,l} = \frac{1}{h_n^{\alpha_x} h_l^{\alpha_y}} \int_{-1}^{1}\int_{-1}^{1} (1-x^2)^{\alpha_x - \frac{1}{2}} (1-y^2)^{\alpha_y - \frac{1}{2}} C_n^{\alpha_x}(x) C_l^{\alpha_y}(y) f_N(x,y)\, dx dy. \tag{76}$$

5.2 Subdomains $\Omega_s = [a_x, b_x] \times [a_y, b_y] \subset [0, L]^2$

Consider the computational domain $[0, L]^2$. Define a set of grids $x_i = \frac{Li}{N_x} (i = 0, ..., N_x - 1)$ and $y_j = \frac{Lj}{N_y} (j = 0, ..., N_y - 1)$. Now, assume that the point values $f(x_i, y_j)$ are known but the function $f(x, y)$ is not. Then the discrete Fourier coefficients $\tilde{f}_{k_x,k_y}$, $-\frac{N}{2} \le k_x, k_y \le \frac{N}{2} - 1$ are obtained by

$$\tilde{f}_{k_x,k_y} = \sum_{i=0}^{N-1}\sum_{j=0}^{N-1} f(x_i, y_j) e^{-i\frac{2\pi k_x}{L} x_i} e^{-i\frac{2\pi k_y}{L} y_j}, \tag{77}$$

and the two-dimensional Fourier finite sum everywhere in $\Omega = [0, L]^2$ is

$$f_N(x, y) = \sum_{k_x=-\frac{N}{2}}^{\frac{N}{2}-1} \sum_{k_y=-\frac{N}{2}}^{\frac{N}{2}-1} \tilde{f}_{k_x,k_y} e^{i\frac{2\pi k_x}{L} x} e^{i\frac{2\pi k_y}{L} y}. \tag{78}$$

Let us denote a subdomain by $\Omega_{s,t} = [a_x, b_x] \times [a_y, b_y]$, where a_x and b_x are the known discontinuities in x-direction and a_y and b_y in y-direction. Define local variables, for $\xi, \eta \in [-1, 1] \times [-1, 1]$, $x^s = \frac{(b_x - a_x)}{2}\xi + \frac{(b_x + a_x)}{2}$ and $y^t = \frac{(b_y - a_y)}{2}\eta + \frac{(b_y + a_y)}{2}$. Let $\epsilon_x = \frac{b_x - a_x}{L}$, $\delta_x = \frac{b_x + a_x}{L}$, $\epsilon_y = \frac{b_y - a_y}{L}$ and $\delta_y = \frac{b_y + a_y}{L}$. Then the Fourier finite sum in the subdomain Ω_s is expressed by

$$f_N(x^s(\xi), y^t(\eta)) = \sum_{k_x=-\frac{N}{2}}^{\frac{N}{2}-1} \sum_{k_y=-\frac{N}{2}}^{\frac{N}{2}-1} \tilde{f}_{k_x,k_y} e^{i\pi k_x(\epsilon_x \xi + \delta_x)} e^{i\pi k_y(\epsilon_y \eta + \delta_y)}. \tag{79}$$

Plugging (77) into (79), we have

$$\begin{aligned} f_N(x^s(\xi), y^t(\eta)) &= \sum_{k_y=-\frac{N}{2}}^{\frac{N}{2}-1} \sum_{j=0}^{N-1} \left[\sum_{k_x=-\frac{N}{2}}^{\frac{N}{2}-1} \left(\sum_{i=0}^{N-1} f(x_i, y_j) e^{-i\frac{2\pi k_x}{L} x_i} \right) e^{i\pi k_x x^s(\xi)} \right] e^{-i\frac{2\pi k_y}{L} y_j} e^{i\pi k_y y^t(\eta)} \\ &= \sum_{k_y=-\frac{N}{2}}^{\frac{N}{2}-1} \left(\sum_{j=0}^{N-1} f_N(x^s(\xi), y_j) e^{-i\frac{2\pi k_y}{L} y_j} \right) e^{i\pi k_y y^t(\eta)}, \end{aligned} \tag{80}$$

and the Gegenbauer coefficients in the subdomain Ω_s have the form

$$b_{n,l}^{\Omega_{s,t}} = \frac{1}{h_l^{\alpha_y}} \int_{-1}^{1} (1-y^2)^{\alpha_y - \frac{1}{2}} C_l^{\alpha_y}(\eta) \left[\sum_{k_y=-\frac{N}{2}}^{\frac{N}{2}-1} \left(\sum_{j=0}^{N-1} \mathbf{b}_l^{\Omega_s}(n, y_j) e^{-i\frac{2\pi k_y}{L} y_j} \right) e^{i\pi k_y y^t(\eta)} \right] d\eta, \tag{81}$$

where

$$\mathbf{b}_l^{\Omega_s}(n, y_j) = \frac{1}{h_l^{\alpha_x}} \int_{-1}^{1} (1-\xi^2)^{\alpha_x - \frac{1}{2}} C_n^{\alpha_x}(\xi) f_N(x^s(\xi), y_j) d\xi. \tag{82}$$

Then, for a fixed y_j, the one-dimensional Gegenbauer reconstruction in the x-direction is written as

$$\mathbf{g}_l^{\Omega_{s,t}}(x^s(\xi), y_j) = \sum_{n=0}^{M_x} \mathbf{b}_l^{\Omega_s}(n, y_j) C_n^{\alpha_x}(\xi). \tag{83}$$

Finally, the two-dimensional reconstruction form is

$$g^{\Omega_{s,t}}(x^s(\xi), y^t(\eta)) = \sum_{l=0}^{M_y} b_{n,l}^{\Omega_{s,t}} C_l^{\alpha_y}(\eta), \tag{84}$$

where

$$b_{n,l}^{\Omega_{s,t}} = \frac{1}{h_n^{\alpha_y}} \int_{-1}^{1} (1-y^2)^{\alpha_y - \frac{1}{2}} C_l^{\alpha_y}(\eta) \left[\sum_{k_y=-\frac{N}{2}}^{\frac{N}{2}-1} \left(\sum_{j=0}^{N-1} \mathbf{g}_l^{\Omega_{s,t}}(x^s(\xi), y_j) e^{-i\frac{2\pi k_y}{L} y_j} \right) e^{i\pi k_y y^t(\eta)} \right] d\eta.$$

Now (69) and (70), the local Gegenbauer coefficients are given in matrix form as

$$b^{\Omega_{s,t}} = \mathbf{B}_y^{\Omega^t} \tilde{\mathbf{f}} \left(\mathbf{B}_x^{\Omega^s} \right)^T, \tag{85}$$

where $b^{\Omega_{s,t}} = [b_{n,l}^{\Omega_{s,t}}]$, $\tilde{\mathbf{f}} = \tilde{f}_{k_y,k_x}$, $\mathbf{B}_x^{\Omega^s} = [B_{n,k_x}^{\Omega^s}]$, and $\mathbf{B}_y^{\Omega^t} = [B_{l,k_y}^{\Omega^t}]$, as defined in (70). Then the two-dimensional Gegenbauer reconstruction can be summarized in matrix form as follows:

$$\mathbf{g}^{s,t} = [\mathbf{T}_y^t \mathbf{A}_y^t (\mathbf{T}_x^s \mathbf{A}_x^s b^{\Omega_{s,t}})^T]^T = \mathbf{T}_x^s \mathbf{A}_x^s (b^{\Omega_{s,t}})^T (\mathbf{A}_y^t)^T (\mathbf{T}_y^t)^T, \tag{86}$$

where $\mathbf{g}^{s,t} = [g_{i,j}^{\Omega_{s,t}}]^T$, $\mathbf{T}_x^s = [T_{i,m}^s] = [\cos(m(\cos^{-1}\xi_{\mathbf{i}}))]$, and $\mathbf{T}_y^t = [T_{j,m}^t] = [\cos(m(\cos^{-1}\eta_{\mathbf{j}})]$ for $\xi_{\mathbf{i}} = \frac{2}{b_x - a_x}\xi_i^s - \frac{b_x + a_x}{b_x - a_x}$, and $\eta_{\mathbf{j}} = \frac{2}{b_y - a_y}\eta_j^t - \frac{b_y + a_y}{b_y - a_y}$, respectively.

A practical way to perform the two-dimensional reconstruction is that we only need to perform the one–dimensional procedure. The Matlab program for the two–dimensional problem is the same as the one for one–dimensional problem, with a outside "for loop". We first perform a one-dimensional reconstruction, say in the x–direction, obtaining one–dimensional reconstructions of the Fourier data in the other direction (say in the y–direction). We then perform a reconstruction in the other direction:

Step 1. Compute the one-dimensional discrete Fourier coefficients w.r.t. x for a y_j.
Step 2. Compute the first $M+1$ discrete Gegenbauer coefficients in a subdomain.
Step 3. Construct the Gegenbauer finite sum on the grids in the subdomain.
Step 4. Repeat Steps 2–3 in the remaining subdomains, separately, for the fixed y_j.
Step 5. Repeat Steps 1–4 for each y_j, and store all the data for the next step.
Step 6. Compute the one-dimensional discrete Fourier coefficients w.r.t. y for a x_i.
Step 7. Repeat Steps 2–5 for all x_i, separately.

6 Application

We applied the cost-effective Gegenbauer reconstruction technique to the two-dimensional Fourier pseudospectral time-domain solutions obtained by (20)–(24), shown in the first columns of Figures 8–14. The reconstructed results are demonstrated in the second columns of Figures 8–14 associated with the PSTD results. Those figures are for the region within the dotted box in the computational domain shown in Figure 1.

Figures 8–11 show snapshots for the field components E_x and E_y at time = 11.48e-15 sec. The data size in the box is 256×256 in the case of $N_x = 1024$, $N_y = 512$ (i.e., $\Delta x = \Delta y = 1$ nm). The Fourier–pseudospectral solutions show nonphysical oscillations throughout the domain across the cylinder and strong oscillations close to the surface of the nanocylinder. Figures 9 and 11 show the one–dimensional slices of Figure 8, along the specified axes across the cylinder. The vertical dotted lines indicate the metal cylinder interfaces for PSTD results and the subdomain interfaces for the Gegenbauer postprocessed results. Since the Gegenbauer reconstructions should be carried in the region where the solution is smooth, the subdomain interfaces need to include the metal interfaces. Thus one can use three subdomains at minimum in the presence of the cylinder and one subdomain in the absence of the cylinder. Here, for the sake of simplicity, we divide two–dimensional subdomains as shown in Figure 7. The one–dimensional slices show five subdomains in x– and y–direction, respectively. The structure of the PSTD solution is different in different slices and their each subdomain. Thus different parameters for M and α are assigned in each slice and each subdomain. At this stage, the parameters are chosen by observation through numerical experiments. Full reconstructions in two dimensions are shown in the right columns in Figures 8 and 10 and one–dimensional reconstructed results are in the right columns in Figures 9 and 11. The one– and two–dimensional reconstruction results show successful improvement in reducing the oscillations.

The total CPU time of the PSTD simulations for the snapshots of E_x and E_y is 7669.9 sec on an AMD Athlon of 1 GHz. The total CPU times of the Gegenbauer reconstructions for the snapshots of E_x and E_y are 164.40 sec and 164.79 sec, respectively, since the reconstruction parameters are not the same ; see Figures 8 and 10. Note that the postprocessing time is insignificant compared to the total PSTD simulation time. Throughout the additional reconstruction procedure at low–cost, one can successfully extract highly reliable results.

Often one Fourier transforms the time–domain results to obtain frequency–domain results, available over a range of frequencies from one time–domain simulation. Such frequency–domain results are useful for many purposes, including estimating optical spectra. Figure 12–14 display the absolute magnitude of the time-averaged electric field corresponding to $\omega = \frac{2\pi c}{\lambda}$ Hz, $\lambda = 340$ nm. The first columns in Figure 12–14 show the PSTD results for the case of $\Delta x = \Delta y = 0.5$ nm. The second columns show the Gegenbauer reconstructions to the Fourier data $N = 512$ from PSTD results. We divide two–dimensional subdomains in a similar manner as in Figure 7. In the third columns, we also present FDTD results inferred with a much smaller grid spacing of 0.1 nm. Taking a close look at the one–dimensional slices in Figure 13 and 14, we observe that FDTD does not suffer much from Gibbs oscillations away from the metal surface/air interfaces and it converges to better than 5% accuracy(excluding the metal surface boundaries). However, near the metal surface/air interfaces, oscillations are observed. Remarkably, the Gegenbauer–postprocessed results with the PSTD data size $N = 512$ eliminate the non–physical oscillations of the original PSTD calculation and the reconstructed results agree well with the finer resolution FDTD results aways from the metal boundary. Moreover, one can confirm that the Gegenbauer-postprocessed results successfully capture reasonable profiles of the field response *up to* the metal interfaces whereas FDTD results does not : see Figures 13 and 14.

7 Discussion

Parameter optimization is important for the Gegenbauer reconstruction technique to be useful in practice. In this problem, for the one–dimensional reconstructions in the absence of the cylinder, $\alpha = 1$ or 2 and $M = 10$–20 were chosen. For the one–dimensional reconstructions in the presence of the cylinder, it required relatively larger α such as $\alpha = 6$–18 and relatively smaller M such as $M = 6$–10: see Figures 9 and 11. Similar pattern has been applied for the reconstructed results shown in Figure 12-14. Thus one might obtain

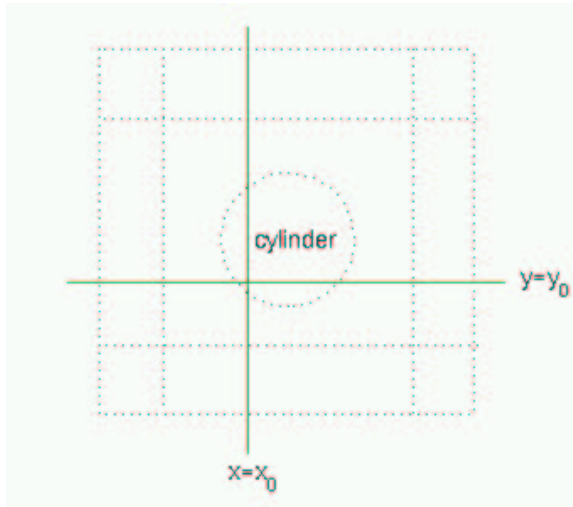

Figure 7: Subdomains in two dimensions : solid lines are the one–dimensional slices and dotted lines are the interfaces of the subdomains.

consistent results, in general, by choosing relatively small α and large M for smooth region and relatively large α and small M in the subdomains adjacent to discontinuities.

Accordingly, we introduce an idea to implement an automated reconstruction algorithm which automatically assigns optimized parameters during reconstruction procedure. From the observation of the reconstruction behaviors depending on M and α and the lesser sensitivity with changing the size of the subdomains, we might fix parameters a priori for more structured region and relatively smooth region in different way.

Then, with the initially given parameters, we might be able to carry out the reconstructions until they give better resolutions by changing the parameters or adjusting the number(or sizes) of subdomains near the discontinuities. In order to measure the improvement of the reconstructed solutions, we consider using smooth indicators from the WENO method [28]. This idea will be further discussed in a future paper.

8 Conclusion

We have presented a cost-effective Gegenbauer reconstruction technique applicable when one has a priori knowledge of the problem discontinuities. In one dimension, exponential convergence of the Gegenbauer reconstructions was demonstrated for a nonperiodic and some piecewise analytic functions. We extended the method to two dimensions and applied it as a postprocessing to the oscillatory Fourier pseudospectral solutions which simulate electromagnetic waves interacting with a metallic nanowire where strong surface plasmon excitations can occur. Successful reduction of the oscillations in Fourier pseudospectral solutions are obtained after the Gegenbauer reconstructions. Comparisons of the reconstructed results to a finer resolution FDTD result are also provided. Surprisingly, the Gegenbauer reconstructions provide reasonable profiles of the field response *up to* the metal surface in contrast with the finer resolution FDTD results.

Further development to seek an automated parameter–optimizing reconstruction method is an important goal for future work.

References

[1] M. Abramowitz, I.A. Stegun, Handbook of mathematical functions, Dover Publications, Inc., New York, 1970.

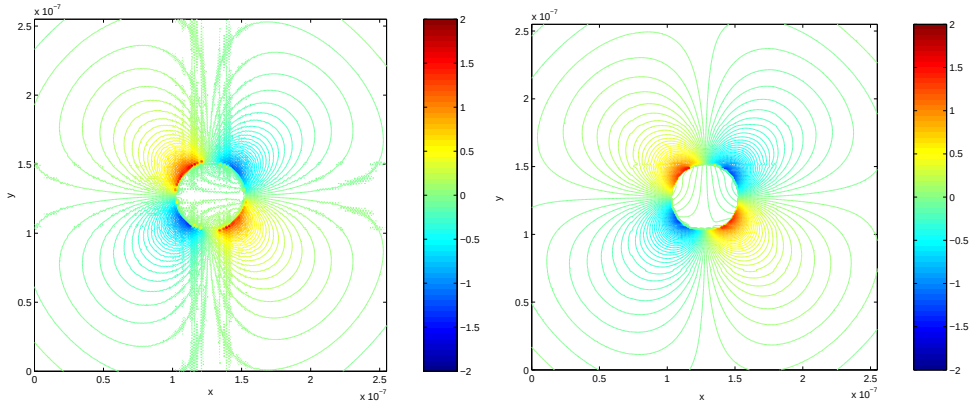

Figure 8: Snapshots of E_x at time = 11.48e-15 sec with Δt =1.3514e-18 : From the left, PSTD solution(CPU time=7669.9 sec) and Gegenbauer reconstruction (CPU time=164.40 sec) computed on an AMD Athlon of 1 GHz).

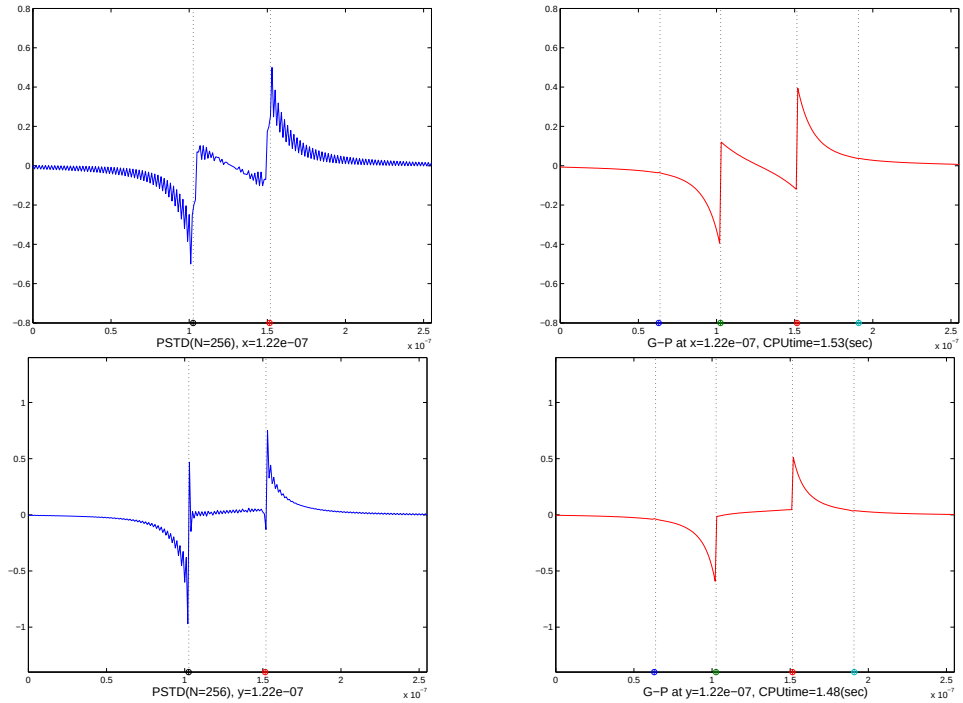

Figure 9: One-dimensional slices of E_x: Dotted lines indicate the interfaces of the cylinder for the spectral (PSTD: left column) solution and the interfaces of subdomains for the Gegenbauer postprocessed (Gegenbauer: right column) solution. Parameters for Gegenbauer are chosen as $M = 7, 7, 4, 7, 7$ for five subdomains from left to right with a fixed $\alpha = 16$.

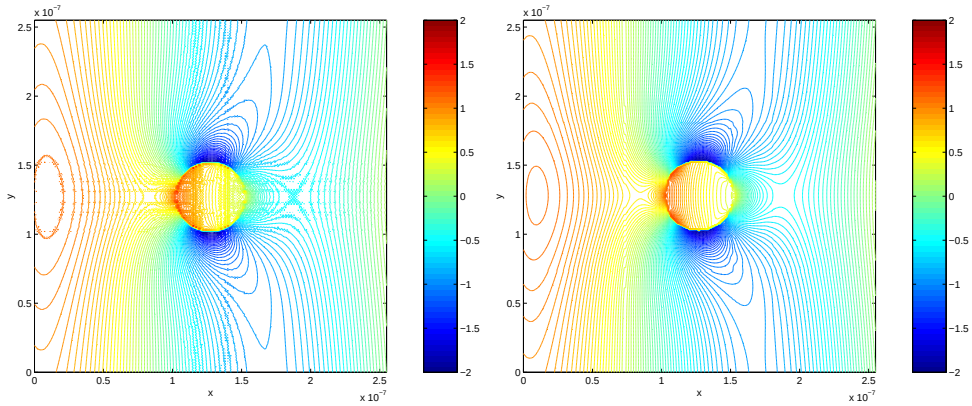

Figure 10: Snapshots of E_y at time = 11.48e-15 sec with Δt =1.3514e-18: From the left, PSTD solution (CPU time=7669.9 sec) and Gegenbauer reconstruction (CPU time = 164.79 sec) computed on an AMD Athlon of 1 GHz).

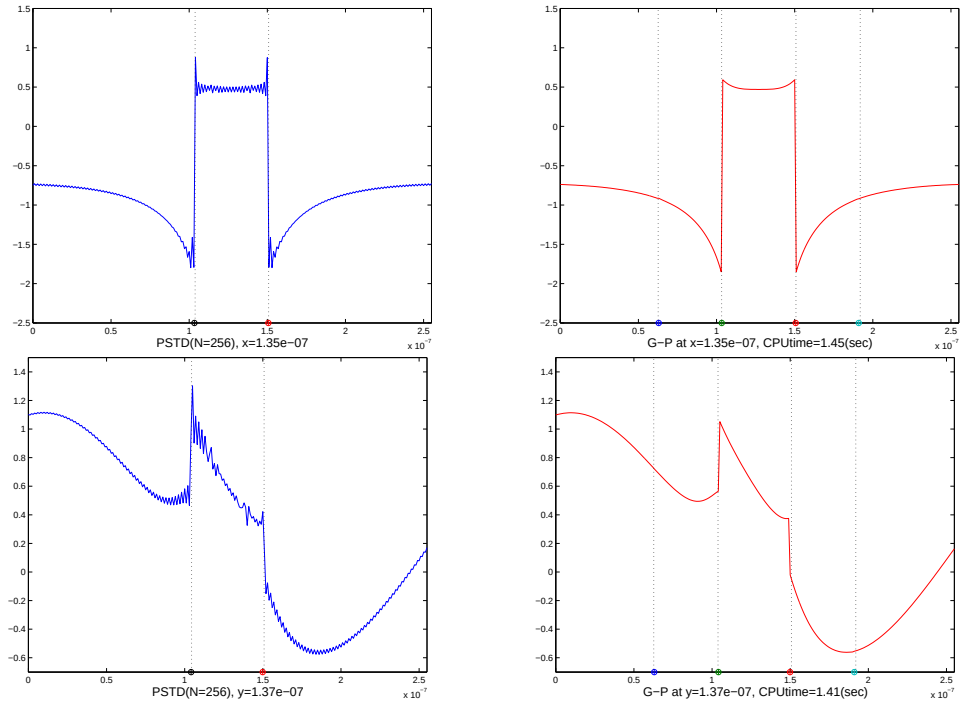

Figure 11: One-dimensional slices of E_y: Dotted lines indicate the interfaces of the cylinder for the spectral (PSTD: left column) solution and the interfaces of subdomains for the Gegenbauer postprocessed (Gegenbauer: right column) solution. Parameters for Gegenbauer are chosen as $M = 5, 5, 3, 5, 5$ for five subdomains from left to right with a fixed $\alpha = 18$.

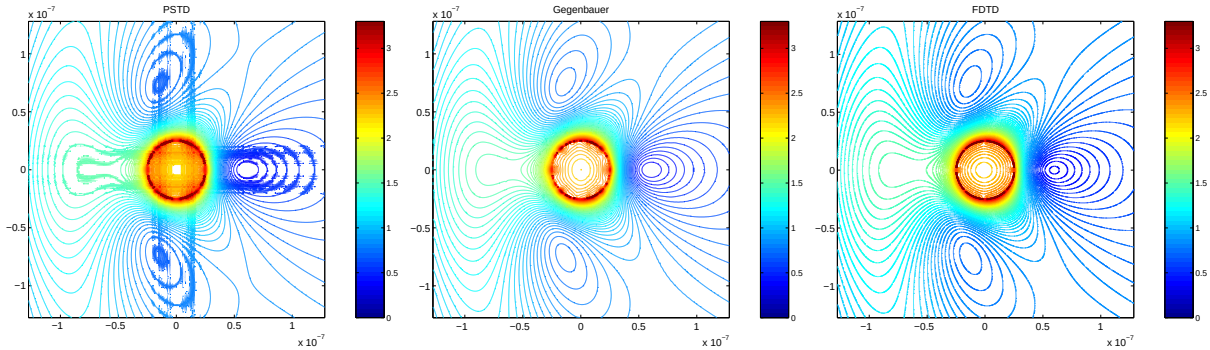

Figure 12: Distributions of time-averaged electric field $|\tilde{E}|$: PSTD (left) and Gegenbauer (middle) with $\Delta x = \Delta y = 0.5$ nm and FDTD (right) with $\Delta x = 0.1$ nm.

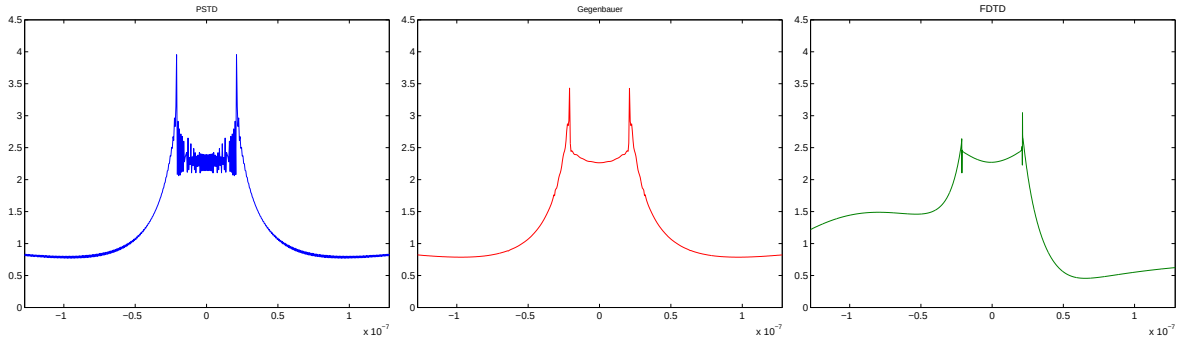

Figure 13: One–dimensional slices in x–direction of the distributions of time-averaged electric field $|\tilde{E}|$: PSTD (left) and Gegenbauer (middle) with $\Delta x = \Delta y = 0.5$ nm, and FDTD (right) with $\Delta x = \Delta y = 0.1$ nm.

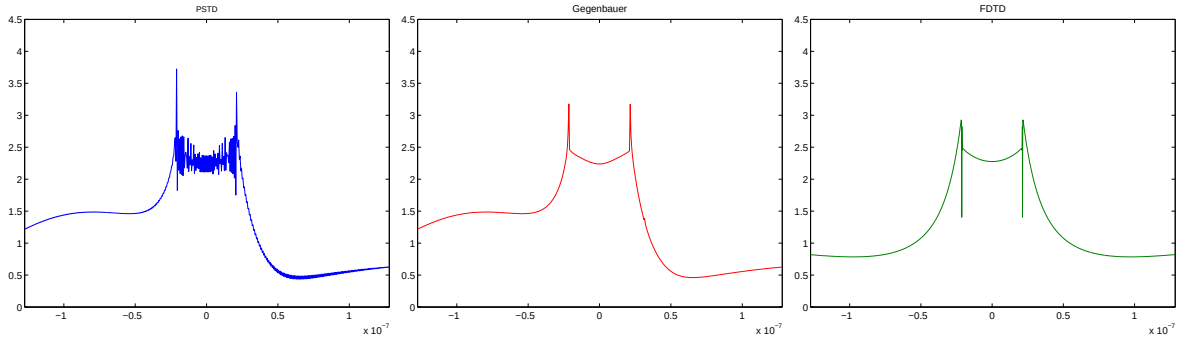

Figure 14: One–dimensional slices in y–direction of the distributions of time-averaged electric field $|\tilde{E}|$: PSTD (left) and Gegenbauer (middle) with $\Delta x = \Delta y = 0.5$ nm, and FDTD (right) with $\Delta x = \Delta y = 0.1$ nm.

[2] W.L. Barnes, A. Dereux, and T.W. Ebbensen, Surface plasmon subwavelength optics, Nature 424, pp. 824–830, 2003.

[3] H. Bateman, Higher transcendental functions, Vol. 2. McGraw-Hill, New York, 1953.

[4] C.F. Bohren, D.R. Huffman, Absorption and scattering of light by small particles, John Wiley & Sons, Inc., New York, 1998.

[5] M.O. Deville, P.F. Fischer, E.H. Mund, High-order methods for incompressible fluid flow, Cambridge University Press, Cambridge, UK, 2002.

[6] D. Funaro, Polynomial approximation of differential equations, Springer-Verlag, New York, 1991.

[7] B. Gustafsson, H. Kreiss and J. Oliger, Time dependent problems and difference methods, Wiley, 1995.

[8] S.G. Johnson, J.D. Joannopoulos, Block–iterative frequency–domain methods for Maxwell's equations in a planewave basis, Optics Express, Vol. 8, No. 3, pp. 173–190, 2001.

[9] Q.H. Liu, Large-scale simulations of electromagnetic and acoustic measurements using the pseudo-spectral time-domain (PSTD) algorithm, IEEE Trans. Geosci. Remote Sensing, 37, pp. 917–926, 1999.

[10] C. Mias, J.P. Webb, R.L. Ferrari, Finite element modelling of electromagnetic waves in doubly and triply periodic structures, IEE Proc. Optoelectron, 146, no. 2, pp. 111–118, 1999.

[11] J. Gibbs, Fourier's series, letter in Nature, 59, p. 200, 1898.

[12] D. Gottlieb, M.Y. Hussaini, S. Orszag, Theory and applications of spectral methods, in Spectral methods for partial differential equations, edited by R. G. Voigt, D. Gottlieb, and M. Y. Hussaini, SIAM, Philadelphia, 1984.

[13] D. Gottlieb, S. Orszag, Numerical analysis of spectral methods: theory and applications, CBMS-NSF Regional Conference Series in Applied Mathenatics, SIAM, Philadelphia, 1977.

[14] D. Gottlieb, C.W. Shu, On the Gibbs phenomenon IV: Recovering exponential accuracy in a sub-interval from a Gegenbauer partial sum of a piecewise analytic function, Mathematics of Computation, 64, pp. 1081–1095, 1995.

[15] D. Gottlieb, C.W. Shu, On the Gibbs phenomenon and its resolution, SIAM Review, 30, pp. 644–668, 1997.

[16] S. Abarbanel, D. Gottlieb, A mathematical analysis of the PML method, J. Comput. Phys. 134, pp. 357–363, 1997.

[17] S.K. Gray, T. Kupka Propagation of light in metallic nanowire arrays: Finite-difference time domain studies of silver cylinders, Physical Review B, 68, pp. 045415/1–045415/11, 2003.

[18] J.M. Oliva, S.K. Gray Theoretical study of dielectrically coated metallic nanowires, Chemical Physics Letters, 379, pp. 325–331, 2003.

[19] J.S. Hesthaven, D. Gottlieb, Spectral approximation of partial differential equations: Numerical analysis and applications, Lecture Notes, Brown University, 1996.

[20] T.W. Lee, S.C. Hagness Pseudo-spectral time domain methods for modeling optical wave propagation in second order nonlinear materials, J. Optical Society of America B, 21, pp. 330-342, 2004.

[21] T.W. Lee, S.C. Hagness A compact wave source condition for the pseudospectral time-domain method, IEEE Trans. Antennas Wireless Propag. Lett., 2004 (accepted).

[22] S.A. Maier, P.G. Kik, H.A. Atwater, S. Meltzer, E. Harel, B. E. Kowel, A. A. G. Requicha, Local detection of electromagnetic energy transport below the diffraction limit in metal nanoparticle plasmon waveguides, Nature Materials 2, pp. 229–232, 2003.

[23] M.S. Min, Spectral method for discontinuous problems, Ph.D. thesis, Brown University, 2002.

[24] M.S. Min, C.H. Teng, The instability of the Yee scheme for the "magic time step", J. Comput. Phys. 166 (2): 418-424, 2001.

[25] M.S. Min, D. Gottlieb, On the convergence of the Fourier approximation for eigenvalues and eigenfunctions of discontinuous problems, SIAM J. Numer. Anal. 40, no. 6, pp. 2254–2269, 2003

[26] M.S. Min, S.M. Kaber, W.S. Don, Fourier-Padé approximations and filtering for the spectral simulations of incompressible Boussinesq convection problem, Math. Comp., 2004 (accepted).

[27] Z.S. Sacks, D.M. Kingsland, R. Lee, J.F. Lee A perfectly matched anisotropic absorber for use as an absorbing boundary condition, IEEE Trans. Antennas Propag., 43, no. 12, pp. 1460–1463, 1995.

[28] C.W. Shu Essentially non-oscillatory and weighted essentially non-oscillatory schemes for hyperbolic conservation laws, ICASE Report No. 97-65, 1997.

[29] A. Taflove, S.C. Hagness, Computational electrodynamics, the finite difference time domain method, Artech House, Norwood, MA, 2000.

[30] K.S. Yee, Numerical solution of initial boundary value problems involving Maxwell's equations in isotropic media, IEEE Trans. Antennas Propag., AP-14, pp. 302–307, 1966.

The submitted manuscript has been created by the University of Chicago as Operator of Argonne National Laboratory ("Argonne") under Contract No. W-31-109-ENG-38. The U.S. Government retains for itself, and others acting on its behalf, a paid-up, nonexclusive, irrevocable worldwide license in said article to reproduce, prepare derivative works, distribute copies to the public, and perform publicly and display publicly, by or on behalf of the Government.